In vitro reconstitution of T cell receptor-mediated segregation of the CD45 phosphatase

Catherine B. Carbone[a,b,c], Nadja Kern[a,b], Ricardo A. Fernandes[d,e,f], Enfu Hui[a,b,c,1], Xiaolei Su[a,b,c], K. Christopher Garcia[d,e,f], and Ronald D. Vale[a,b,c,2]

[a]Department of Cellular and Molecular Pharmacology, University of California, San Francisco, CA 94158; [b]Howard Hughes Medical Institute, University of California, San Francisco, CA 94158; [c]Howard Hughes Medical Institute Summer Institute, Marine Biological Laboratory, Woods Hole, MA 02543; [d]Department of Molecular and Cellular Physiology, Stanford University School of Medicine, Stanford, CA 94305; [e]Department of Structural Biology, Stanford University School of Medicine, Stanford, CA 94305; and [f]Howard Hughes Medical Institute, Stanford University Medical School, Stanford, CA 94305

Contributed by Ronald D. Vale, September 13, 2017 (sent for review June 8, 2017; reviewed by Michael L. Dustin and Daniel A. Fletcher)

T cell signaling initiates upon the binding of peptide-loaded MHC (pMHC) on an antigen-presenting cell to the T cell receptor (TCR) on a T cell. TCR phosphorylation in response to pMHC binding is accompanied by segregation of the transmembrane phosphatase CD45 away from TCR–pMHC complexes. The kinetic segregation hypothesis proposes that CD45 exclusion shifts the local kinase–phosphatase balance to favor TCR phosphorylation. Spatial partitioning may arise from the size difference between the large CD45 extracellular domain and the smaller TCR–pMHC complex, although parsing potential contributions of extracellular protein size, actin activity, and lipid domains is difficult in living cells. Here, we reconstitute segregation of CD45 from bound receptor–ligand pairs using purified proteins on model membranes. Using a model receptor–ligand pair (FRB–FKBP), we first test physical and computational predictions for protein organization at membrane interfaces. We then show that the TCR–pMHC interaction causes partial exclusion of CD45. Comparing two developmentally regulated isoforms of CD45, the larger R_{ABC} variant is excluded more rapidly and efficiently (∼50%) than the smaller R_0 isoform (∼20%), suggesting that CD45 isotypes could regulate signaling thresholds in different T cell subtypes. Similar to the sensitivity of T cell signaling, TCR–pMHC interactions with K_ds of ≤15 μM were needed to exclude CD45. We further show that the coreceptor PD-1 with its ligand PD-L1, immunotherapy targets that inhibit T cell signaling, also exclude CD45. These results demonstrate that the binding energies of physiological receptor–ligand pairs on the T cell are sufficient to create spatial organization at membrane–membrane interfaces.

CD45 | TCR | kinetic segregation | signaling | PD-1

Binding of the T cell receptor (TCR) to agonist peptide-MHC (pMHC) triggers a signaling cascade within a T cell leading to reorganization of the cytoskeleton and organelles, transcriptional changes, and cell proliferation. The first step in the cascade is TCR phosphorylation by the Src family tyrosine kinase Lck (2). One model, called "kinetic segregation" (3) for how this initiating phosphorylation is triggered, proposes that the close membrane contact created by TCR–pMHC binding results in exclusion of the transmembrane phosphatase CD45, and the shift of the kinase–phosphatase balance favors net phosphorylation of the TCR by Lck. The basis of this exclusion is thought to be steric, since the large CD45 extracellular domain (CD45 R_0 isoform, 25 nm; CD45 R_{ABC} isoform, 40 nm) (Table S1) (4–6) may not be able to penetrate the narrow intermembrane spacing generated by the TCR–pMHC complex (13 nm) (Table S1) (7, 8).

Imaging T cells activated ex vivo either by B cells (9) or by antigen presented on supported lipid bilayers (SLBs) (10, 11) has revealed that CD45 is indeed partitioned away from the TCR upon pMHC binding. Cellular reconstitutions have demonstrated that the large extracellular domain of CD45 is required for this segregation (12, 13). Additionally, size-dependent segregation of CD45 by orthogonal receptor–ligand pairs that create a similar narrow intermembrane cleft is sufficient for T cell triggering in the absence of TCR–pMHC binding (6, 12).

Despite this strong cellular evidence for size-based partitioning, it has been debated whether the physical properties of CD45 and TCR–pMHC at the membrane–membrane interface alone are sufficient to explain the observed segregation behavior or whether other cellular factors (e.g., actin cytoskeletal or lipid ordering) are also required. Several groups have computationally modeled aspects of size-based organization at membrane interfaces, and two independent mathematical approaches have concluded that spontaneous pattern formation can occur in physiological parameter ranges (14, 15). These models predict the contributions of protein (size, concentration, elasticity, affinity, and kinetics), membrane (stiffness, tension, repulsion), and environmental (thermal fluctuations, cytoskeleton, time) factors in regulating partitioning. Although these models focus primarily on a system with two binding pairs (TCR–pMHC and ICAM-1–LFA-1), some of the predictions can be extrapolated to a system with both ligand-bound and unbound species.

Successful efforts to reconstitute molecular segregation at membrane–membrane interfaces have been made with dimerizing GFP molecules (16) and hybridizing strands of DNA (17). These

Significance

The T cell receptor (TCR) and PD-1 signaling cascades have been hypothesized to be triggered by the exclusion of the transmembrane phosphatase CD45 from sites of receptor–ligand engagement at the T cell–antigen-presenting cell interface. We reconstituted TCR–pMHC– and PD1–PD-L1–mediated segregation of CD45 with purified proteins and model membranes, demonstrating that this phenomenon can occur in the absence of any active cellular organization. In this minimal system, two developmentally regulated and different size isoforms of CD45 are differently segregated by TCR–pMHC binding, suggesting a possible mechanism for the fine-tuning of signaling. Collectively, our data show that the binding energy of physiological receptor–ligand pairs is sufficient to create spatial organization in membranes.

This work was posted earlier as a preprint (1).

Author contributions: C.B.C., N.K., E.H., X.S., and R.D.V. designed research; C.B.C., N.K., and E.H. performed research; C.B.C., N.K., R.A.F., E.H., X.S., and K.C.G. contributed new reagents/analytic tools; C.B.C. and N.K. analyzed data; and C.B.C., N.K., and R.D.V. wrote the paper.

Reviewers: M.L.D., Kennedy Institute of Rheumatology; and D.A.F., University of California, Berkeley.

The authors declare no conflict of interest.

[1]Present address: Division of Biological Sciences, Cell and Developmental Biology, University of California, San Diego, La Jolla, CA 92093.

[2]To whom correspondence should be addressed. Email: ron.vale@ucsf.edu.

This article contains supporting information online at www.pnas.org/lookup/suppl/doi:10.1073/pnas.1710358114/-/DCSupplemental.

studies show that laterally mobile molecules at membrane–membrane interfaces organize by height and locally deform the membrane to accommodate different molecular sizes. However, results from high-affinity, artificial receptor–ligand pairs cannot be simply extrapolated to predict results for physiologically relevant molecules at the T cell–APC interface. Here, we have recapitulated TCR–pMHC–mediated partitioning of CD45 on model membranes.

Results

A Chemically Inducible Receptor–Ligand System for Producing CD45 Exclusion at a Membrane–Membrane Interface. To mimic a T cell, we used a giant unilamellar vesicle (GUV) containing a nickel-chelating lipid to which a purified His-tagged, fluorescently labeled receptor and CD45 could be added (Fig. 1*A*). To mimic the antigen-presenting cell (APC), we used an SLB containing nickel-chelating lipids to which a His-tagged protein ligand also could be bound. All proteins were linked to their target membrane via either His_{10} or His_{12}, as detailed in *Methods*. As an initial test of this system, we used an artificial receptor (FKBP) and ligand (FRB) that could be induced to form a tight binding interaction (100 fM) upon the addition of rapamycin (18). To maintain the GUV and SLB in proximity before rapamycin addition, the two membranes were passively tethered to one another using two 100mer single-stranded DNA molecules with a 20-bp region of complementarity (Table S1) (19, 20). The elongated extracellular domain of the CD45 R_0 isoform (25 nm) (4–6) and the smaller SNAP protein (5 nm) (Table S1) (21) were used as test proteins for partitioning.

Upon rapamycin addition, FKBP and FRB concentrated first in small micrometer-scale clusters at the GUV–SLB interface, which then grew in size over the interface; simultaneously, fluorescently labeled CD45 R_0 partitioned away from regions of the GUV that became enriched in receptor–ligand pairs (Fig. 1*B* and Movie S1). In contrast to CD45, which was strongly depleted by FRB–FKBP, the SNAP protein (5 nm) (Protein Data Bank ID code 3KZY) or a lipid dye (Atto390-DOPE) remained evenly distributed throughout the interface after rapamycin addition (Fig. 1 *C* and *D*). We also tested PD-L1 (8 nm) (Table S1), which also remained evenly distributed throughout the interface after rapamycin addition (Fig. S1). The size of FKBP–FRB clusters could be varied by changing the receptor concentration on the GUV membrane;

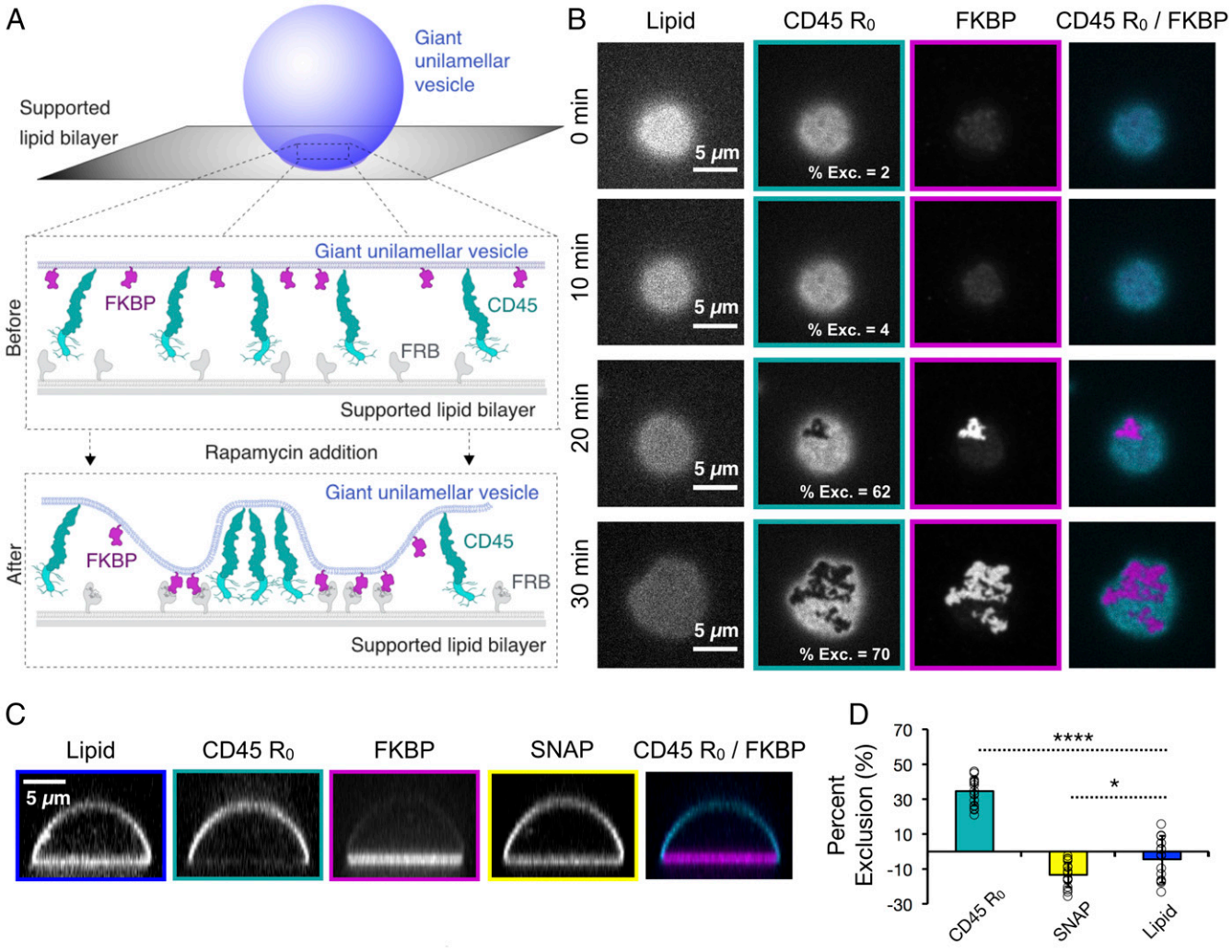

Fig. 1. Receptor–ligand binding induces CD45 segregation at membrane interfaces. (*A*) Schematic of rapamycin-induced receptor–ligand (FKBP–FRB) binding and CD45 R_0 segregation between a GUV and an SLB. (*B*) TIRF microscopy of a GUV–SLB interface at the indicated times after rapamycin addition, showing the concentration of FKBP into microdomains that exclude CD45 R_0. The percent of CD45 R_0 exclusion is indicated for each image shown. (*C*) Spinning-disk z-sections of GUVs after membrane-apposed interfaces have reached equilibrium, showing localization of FKBP to the membrane interface, localization of CD45 R_0 away from the interface, and uniform distribution of SNAP. (*D*) Quantification of experiment shown in *C*; data are shown as mean ± SD ($n = 17$ GUVs pooled from two experiments). *$P < 0.05$; ****$P < 0.0001$; *t* test.

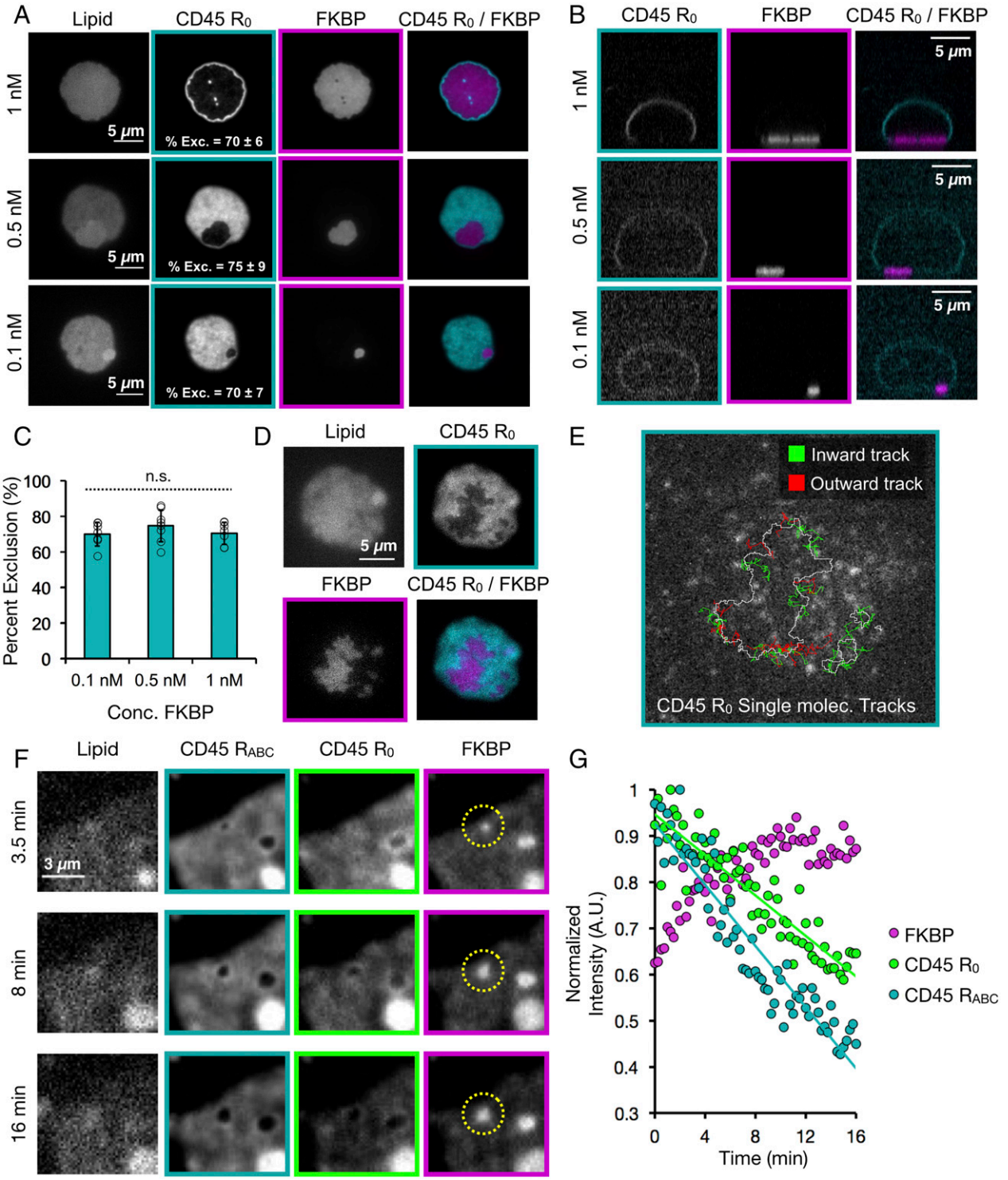

Fig. 2. Characterization of partitioned GUV–SLB membrane–membrane interfaces. (*A*) Titration of FKBP concentration (indicated at the left of the images) with a constant CD45 R_0 concentration imaged by TIRF microscopy. The percent of CD45 R_0 exclusion is indicated as mean ± SD with $n = 7$ or 8 GUVs per condition pooled from three experiments. (*B*) Spinning-disk z-sections of GUVs shown in *A*. (*C*) Graphical representation of data shown in *A*; n.s., not significant (*D*) TIRF microscopy of a GUV–SLB interface showing the overall localization of CD45 R_0 and FKBP. (*E*) Single-molecule imaging of CD45 R_0 for the GUV shown in *D*. The border of the FKBP-enriched zone is indicated by a white line. Only tracks crossing the exclusion boundary are shown. CD45 R_0 single-molecule tracks originating outside the FKBP-enriched zone are shown as green lines, and tracks originating inside the FKBP-enriched zone are shown as red lines. (*F*) TIRF microscopy of a GUV–SLB interface at 30-s time points after rapamycin addition showing the concentration of FKBP into microdomains that exclude CD45 R_0 and CD45 R_{ABC}. The rate of CD45 R_{ABC} exclusion is 2.8 ± 0.9 times faster than rate of CD45 R_0 exclusion; $n = 7$ GUVs from two experiments. (*G*) Quantification of exclusion for the representative GUV shown in *F*.

however, the degree of CD45 R_0 exclusion from clusters was similar over the range tested (Fig. 2 *A*–*C*). Across all concentrations of FKBP, at receptor–ligand–enriched zones, CD45 R_0 was depleted by 72 ± 7% ($n = 22$ GUVs pooled from two experiments). Once

formed, the receptor-enriched and -depleted zones stably retained their shapes for tens of minutes, and receptor–ligand pairs in the enriched zones were largely immobile, as evidenced by fluorescence recovery after photobleaching (FRAP) (Fig. S2). However, using single-molecule total internal reflection fluorescence (TIRF) imaging, we observed that single molecules of CD45 R_0 can diffuse across FKBP–FRB–enriched and –depleted zones (Fig. 2 *D* and *E* and Movie S2). This result reveals that individual molecules can move across these micrometer-scale boundaries.

In addition to testing the CD45 R_0 isoform for segregation, we also compared the extracellular domain of the CD45 R_{ABC} isoform, which is preferentially expressed early in T cell development (22) and is about 15 nm larger than the shorter and later-expressed R_0 isoform (Table S1) (4, 5). With both isoforms present on the same GUV, the larger CD45 R_{ABC} isoform segregated from newly forming FKBP clusters threefold faster than the R_0 isoform (2.8 ± 0.9-fold, n = 7 GUVs pooled from two experiments) (Fig. 2 *F* and *G* and Movie S3). However, the final extent of the exclusion of the two CD45 isoforms was similar with this high-affinity FRB–FKBP system (Fig. S3).

The kinetic segregation model predicts that CD45 is excluded from receptor–ligand complexes based upon a difference in the spacing between the GUV and SLB in the receptor- versus CD45-enriched regions (3). To investigate the topology of the GUV membrane across the interface with nanometer accuracy in the vertical axis, we used scanning angle interference microscopy (SAIM), a technique that calculates the distance of fluorophores from a silicon oxide wafer by collecting sequential images at multiple illumination angles (Fig. 3*A*) (23). The SAIM reconstructions revealed membrane deformations at regions of CD45 localization (Fig. 3 *B*–*D*). The calculated difference in membrane spacing between the FRB–FKBP– and CD45 R_0-enriched regions was 18 ± 11 nm (n = 4–6 regions from each of four GUVs from two experiments, pooled), suggesting a size of ∼24 nm for the CD45 R_0 extracellular domain, assuming that FRB–FKBP creates an intermembrane space of 6 nm (Table S1) (24). This value is similar to the ∼22-nm axial dimension for the CD45 R_0 extracellular domain determined by electron microscopy (6). Conversely, for GUV–SLB interfaces with FRB–FKBP and SNAP, SAIM reconstructions revealed no changes in membrane spacing across the GUV–SLB interface (Fig. 3 *E*–*G*).

TCR–pMHC–Mediated CD45 Exclusion. Next, we sought to establish a GUV–SLB interface using the native T cell receptor–ligand pair, TCR–pMHC (Fig. 4*A*). For the TCR, we coexpressed the extracellular domains of the 2B4 α and β chains extended with leucine zippers to stabilize their dimerization (25); both chains were tagged with His_{10} for conjugation to the GUV membrane, and the β chain contained a ybbR peptide for fluorescent labeling. For the ligand, we used the IE^k MHC, His_{10}-tagged loaded with a high-affinity (2.5 μM K_d) peptide. Similar to the results previously described for FRB–FKBP, we observed the formation of micron-sized TCR clusters that excluded CD45 R_0 (22 ± 14% exclusion, n = 17 GUVs pooled from two experiments) (Fig. 4*B* and Movie S4) but not the control SNAP domain (Fig. S3*A*).

We also combined both CD45 R_{ABC} and CD45 R_0 isoforms on the same GUV and compared their segregation with the TCR–pMHC system. Upon GUV contact with the SLB, the 2B4 TCR bound the IE^k MHC and concentrated at the interface where it formed micrometer-scale clusters that excluded both isoforms of CD45 (Fig. 4*C*). However, unlike the high-affinity FKBP–FRB system in which the two CD45 isoforms R_0 and R_{ABC} are excluded to a similar level (Fig. S3), the degree of TCR–pMHC–mediated exclusion of the smaller CD45 R_0 isoform (15 ± 7% exclusion) was lower than the larger CD45 R_{ABC} isoform (38 ± 9% exclusion) at steady state (45 min, n = 13 GUVs pooled from two experiments) (Fig. 4*D*).

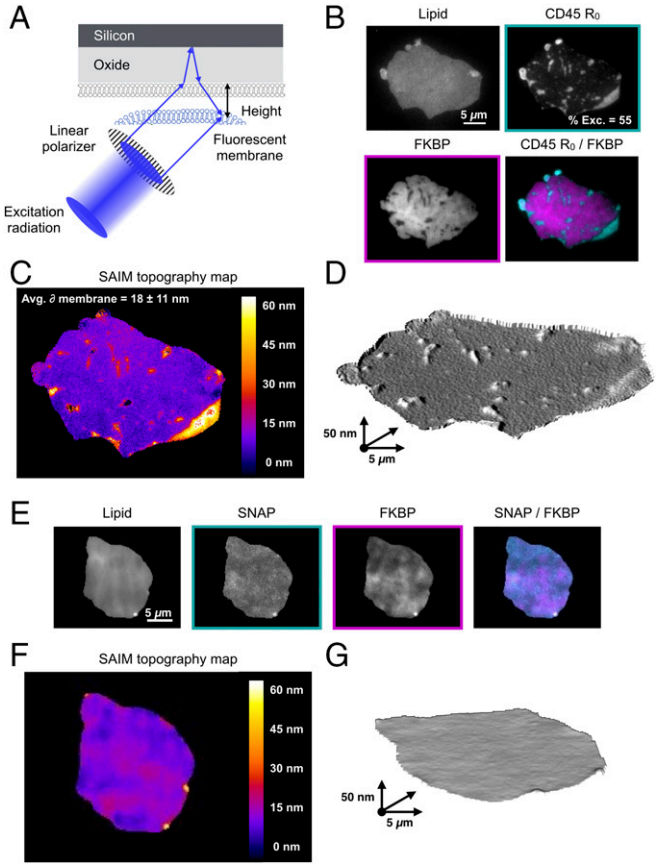

Fig. 3. Membrane topology is influenced by local protein composition. (*A*) Schematic of SAIM showing reflection and interference of excitation light that produces structured illumination patterns used to deduce fluorophore height; adapted from ref. 45. (*B*) Epifluorescence microscopy showing localization of lipid, CD45 R_0, and FKBP on GUV analyzed by SAIM imaging. The percent of CD45 R_0 exclusion is indicated for the image shown. (*C*) SAIM reconstruction of a GUV membrane derived from lipid fluorescence showing an increase in membrane height at CD45 R_0 clusters. The average change in membrane height is depicted as mean ± SD; n = 4–6 clusters from each of four GUVs imaged during two separate experiments. (*D*) 3D model of the data shown in *C*. The *z*-scale is exaggerated to clearly depict membrane deformations. (*E*) Epifluorescence microscopy showing localization of lipid, SNAP, and FKBP on a GUV analyzed by SAIM imaging. (*F*) SAIM reconstruction of a GUV membrane derived from lipid fluorescence. (*G*) 3D model of the data shown in *F*. The *z*-scale is exaggerated to clearly depict membrane deformations.

In vivo, TCR encounters MHCs loaded with a myriad of different peptides; although not absolute, TCR–pMHC affinities of <50 μM are usually required to trigger a signaling response (26). To examine the effect of TCR–pMHC affinity on CD45 R_{ABC} exclusion, we loaded IE^k MHC with a series of well-characterized peptides with resultant 2D K_ds of 2.5 μM, 7.7 μM, 15 μM, 50 μM, and null for the 2B4 TCR (25). At steady state, we observed that pMHCs with affinities to the TCR of 15 μM and lower excluded CD45 R_{ABC} to similar extents (51 ± 7% exclusion, n = 30 GUVs pooled from two experiments) (Fig. 4 *E* and *F*). However, the pMHC with a K_d of 50 μM and IE^k loaded with null peptides did not concentrate TCR at the GUV–SLB interface and did not change the distribution of CD45 R_{ABC} (−1 ± 6% exclusion, n = 20 GUVs pooled from two experiments) (Fig. 4 *E* and *F*). Thus, in agreement with computational predictions (15), CD45 R_{ABC} exclusion was observed over the same range of affinities that are associated with peptide agonists.

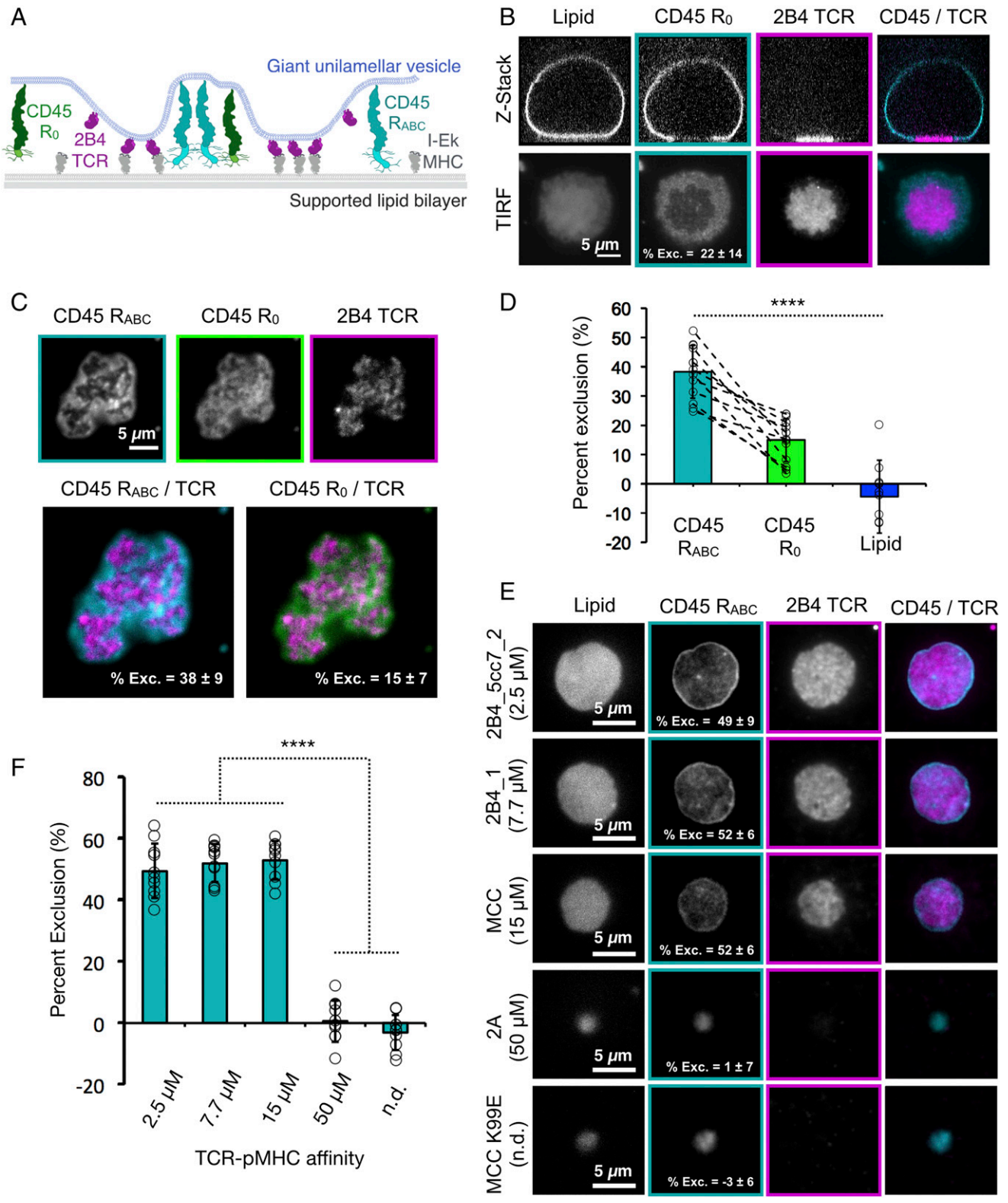

Fig. 4. TCR–pMHC binding induces CD45 segregation at GUV–SLB interfaces. (*A*) Schematic of 2B4 TCR–IE^k MHC binding between a GUV and an SLB and segregating away from two CD45 isoforms (R_0 and R_{ABC}). (*B*, *Upper*) Spinning-disk *z*-sections of GUVs after membrane-apposed interfaces have reached equilibrium, showing localization of 2B4 TCR to the membrane interface and the exclusion of CD45 R_0 away from the interface. (*Lower*) TIRF images of the GUV–SLB interface for the GUV shown in the upper panel. The percent of CD45 R_0 exclusion for the image shown is indicated. (*C*, *Upper*) Segregation of CD45 R_0 and CD45 R_{ABC} on the same GUV membrane away from 2B4 TCR, shown by TIRF microscopy of the membrane interface. (*Lower*) The percent of CD45 isoforms exclusion is indicated as mean ± SD, with $n = 13$ GUVs from two experiments. (*D*) Graphical representation of the data shown in *C*. (*E*) Dependence of CD45 R_{ABC} exclusion as a function of TCR–pMHC affinity using peptides with different K_ds as indicated at the left of the images. Membrane interfaces were imaged by TIRF microscopy. The percent of CD45 R_{ABC} exclusion is indicated as mean ± SD; $n = 10$ GUVs per condition from two experiments. (*F*) Graphical representation of the data shown in *E*; n.d., not detectible. ****$P < 0.0001$; *t* test.

Exclusion of CD45 by PD-1–PD-L1. T cell signaling involves many receptor–ligand pairs interacting across the two membranes in addition to the TCR–pMHC pair (27). The coreceptor PD-1 and its ligand PD-L1 create a signaling system that opposes T cell activation by inhibiting CD28 signaling (28, 29). PD-1 ligation also results in microcluster formation on T cells (30). Like the TCR, PD-1 signaling is initiated through receptor tail phosphorylation by Lck (31), and this phosphorylation event may be opposed by the abundant CD45 phosphatase (Fig. S4 *A* and *B*). Therefore, we tested the ability of the PD-1–PD-L1 interaction, which forms a complex of similar dimension (9 nm) to TCR–pMHC (Table S1) (32), to partition CD45 in our in vitro liposome system (Fig. 5*A*). As expected from these physical dimensions, PD-1–PD-L1 interaction at the membrane–membrane interfaces formed micrometer-sized clusters that excluded CD45 R_{ABC} (Fig. 5*B*). The degree of CD45 R_{ABC} exclusion (60 ± 14% exclusion, $n = 14$ GUVs from two experiments) (Fig. 5*B*) was greater than that observed for TCR–pMHC (2.5 μM peptide), which may be explained by the higher affinity of the PD1–PD-L1 interaction (0.77 μM) (33).

We also combined CD45 R_{ABC} with both TCR–pMHC and PD-1–PD-L1. In this dual receptor–ligand system, the two receptor–ligand complexes colocalized, and CD45 R_{ABC} was partitioned away from the combined ligated TCR–PD-1 footprint (Fig. 5*C*). The size (Table S1) and affinity difference between TCR–pMHC and PD-1–PD-L1 may be small enough to not cause partitioning of these receptor–ligands under the conditions tested in our in vitro assay.

Discussion

In this study, we have established an in vitro membrane system that recapitulates receptor–ligand–mediated CD45 exclusion. We have found that the binding energy of physiological receptor–ligand interactions is sufficient for CD45 partitioning at a model membrane–membrane interface. We also show that subtle differences in sizes and affinities of the proteins at the interface can give rise to significant changes in spatial organization and discuss the implications of these findings in more detail below.

Spatial organization of the TCR and CD45 at the immune cell contacts has been proposed to arise by a nucleation-spreading mechanism (15). By imaging an inducible synthetic receptor–ligand–binding interaction in real time, we also conclude that pattern formation arises by the nucleation of small clusters that spread further across the membrane interface over time. These patterns induce changes in membrane topology that reflect the local protein composition and are stable on the order of hours. However, we show that individual molecules can freely move between domains. This result is consistent with previous computational simulations, although these models predict that patterns will relax to a circular geometry to minimize the length of the domain boundaries (15, 34, 35). In our system, as observed for other physical models of partitioning using DNA–DNA hybridization (17) and dimerizing GFP (16), patterns have more complex domain structures. The lack of circular geometry in the experimental systems could be due to small inhomogeneities in the SLB compared with perfectly diffusive computational models. Despite this difference, many physical and computational model systems have converged on nucleation and spreading as a general mechanism by which spatial organization arises at membrane–membrane interfaces.

The mechanism by which receptor–ligand binding induces spatial organization is a subject of active investigation. Our results showing differential exclusion of CD45 R_0 and CD45 R_{ABC} indicate that size-based steric exclusion and membrane deformation are important for exclusion. In addition, protein crowding of receptor–ligand complexes also could provide a driving force for partitioning. Indeed, previous work has shown that patterns formed at analogous membrane–membrane interfaces using dimerizing GFP as the receptor–ligand pair and a small test protein (monomeric Cherry) are due to crowding effects (16). In our system, however, we observe that the small SNAP protein is distributed throughout receptor–ligand–enriched and –depleted zones. These systems employ different proteins at the interface, and it will be interesting to investigate whether specific protein properties (e.g., size, propensity for oligomerization, elasticity, flexibility, packing density of receptor–ligand in partitioned zones, among others) account for these differences in the role of protein crowding in exclusion.

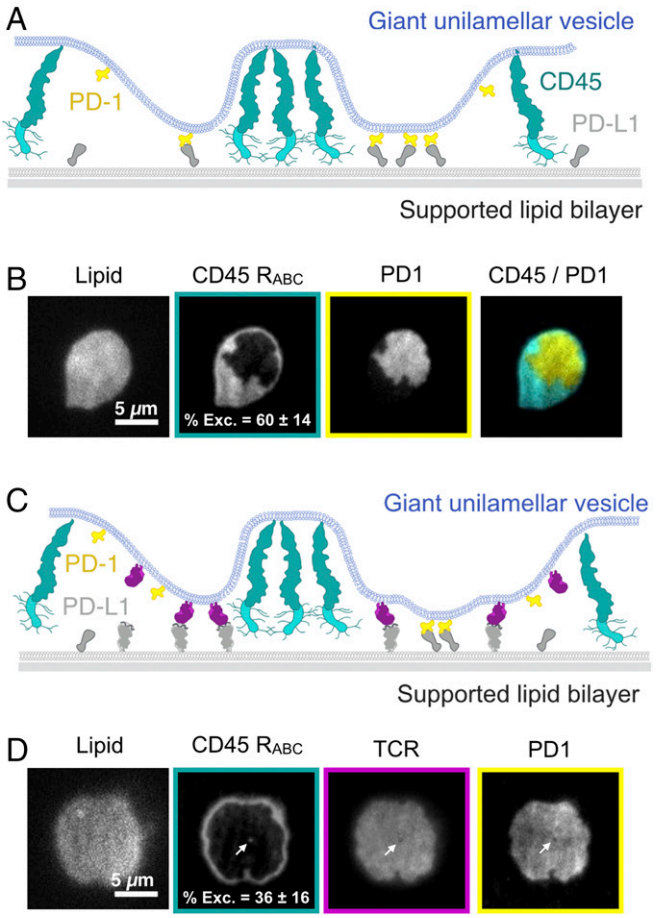

Fig. 5. The inhibitory coreceptor PD-1 excludes CD45 and colocalizes with TCR. (*A*) Schematic of PD-1–PD-L1 binding between a GUV and an SLB, with segregation away from CD45 R_{ABC}. (*B*) TIRF microscopy showing the concentration of PD-1 into microdomains that exclude CD45 R_{ABC}. The percent of CD45 R_{ABC} exclusion is indicated as mean ± SD; $n = 14$ GUVs from two experiments. (C) Schematic of TCR–pMHC and PD-1–PD-L1 induced segregation of CD45 RABC. (*D*) TIRF microscopy showing the concentration of TCR and PD-1 into a domain that excludes CD45 R_{ABC}. The percent of CD45 R_{ABC} exclusion is indicated as mean ± SD; $n = 14$ GUVs from two experiments. White arrows indicate a small CD45 R_{ABC}-enriched zone that is depleted for TCR and PD-1.

Our work also suggests an important contribution of receptor–ligand affinity in protein exclusion. We observed 70% depletion of CD45 R_0 from FRB–FKBP (100 fM K_d)–enriched zones. The TCR–pMHC interactions, on the other hand, are much lower in affinity, with most agonists generally displaying K_ds of 1–100 μM (26). Strikingly, when we tested CD45 exclusion using TCR–pMHC, we found that exclusion was only 22% for the R_0 isoform and 51% for the R_{ABC} isoform when tested individually. The PD-1–PD-L1 interaction is higher affinity (0.7 μM) and produces a somewhat higher exclusion (60%) of CD45 R_{ABC}. While the CD45 R_0 isoform exclusion by TCR–pMHC is modest, it nevertheless could be significant for eliciting a signaling response. In vitro

analysis of the kinase–phosphatase network controlling TCR activation has shown that at physiological protein densities small perturbations of CD45 can drive large changes in TCR phosphorylation (36). In combination with our results, this suggests that the cellular CD45 concentration may position the TCR precisely at the boundary of a switch-like response in phosphorylation.

Our experimental results also are in reasonable agreement with computational predictions for a lower boundary of receptor–ligand affinity needed for protein exclusion. Computational models by Weikl et al. (15) predict that, at the ratio of one TCR molecule to eight CD45 molecules used in these experiments, a binding energy of >4 k_BT (corresponding to a K_d of ∼20 μM) is required for partitioning. In our system, we find that a pMHC ligand with a 15-μM K_d causes CD45 exclusion, whereas a ligand with a K_d of 50 μM does not. It also has been predicted that increasing the affinity of a receptor–ligand interaction should increase the area fraction of the interface occupied by the receptor–ligand–enriched zone by increasing the number of bound complexes at the same protein densities (15, 17). However, in our experiments, TCR–pMHC–mediated CD45 partitioning occurs as an all-or-nothing process.

Our results also demonstrate that the large extracellular domains of CD45 R_{ABC} and CD45 R_0 are differentially sensitive to the partitioning forces produced by ligand–receptor binding interactions at a membrane–membrane interface. This finding is consistent with results showing that T cells expressing larger CD45 isoforms signal more efficiently (37), although others have contested this conclusion (38). Although the signaling consequences of differential CD45 segregation on immune activation remain to be clarified, our results establish a biophysical difference between two highly conserved CD45 isoforms (39) with regard to their degree of spatial segregation in response to TCR–pMHC interactions. Given that the smaller CD45 isoforms are preferentially expressed in later steps of T cell selection (22), our results suggest that T cell signaling may be attenuated by changes CD45 isoform expression as a mechanism of peripheral tolerance.

We also explore increasing complexity at a membrane interface by introducing two receptor–ligand pairs: TCR–pMHC and PD-1–PD-L1. Interestingly, we find that these two receptor–ligand complexes colocalize with one another, and both together exclude CD45. In vivo, partial segregation of these two receptor–ligand pairs also has been observed in $CD8^+$ T cells (28), and a higher degree of colocalization between these receptors was reported in $CD4^+$ T cells (30). Given that the size difference between the TCR–pMHC and PD-1–PD-L1 pairs lies at the biophysical threshold for partitioning (16), these results suggest that cellular localization of PD-1 with respect to TCR may be regulated by other factors (e.g., other coreceptors or adaptor proteins) and perhaps even in a cell type-specific manner. In addition, it will be interesting to investigate how actin polymer dynamics and lipid-mediated organization (40) may enhance or disrupt protein patterning across two membranes.

Materials and Methods

Materials. Synthetic 1,2-dioleoyl-sn-glycero-3-phosphocholine (POPC; Avanti, 850457), 1,2-dioleoyl-sn-glycero-3-[(*N*-(5-amino-1-carboxypentyl)iminodiacetic acid)succinyl] (nickel salt, DGS-NTA-Ni; 790404; Avanti), and 1,2-dioleoyl-sn-glycero-3-phosphoethanolamine-*N* [methoxy(polyethylene glycol)-5000] (ammonium salt, PEG5000-PE; 880220; Avanti) were acquired from Avanti Polar Lipids; 1,2-dioleoyl-sn-glycero-3-phosphoethanolamine-Atto390 (DOPE-390; AD390-161) was acquired from Atto Technology.

Recombinant Protein Expression, Purification, and Labeling. N-terminally His_{10}- and SNAP-tagged FRB and FKBP were subcloned into a pET28a vector and were bacterially expressed in the BL21(DE3) strain of *Escherichia coli*. The cells were lysed in an Avestin EmulsiFlex system. C-terminally His_{10}- and SNAP-tagged extracellular domains of human CD45 R_0, human CD45 R_{ABC}, and human PD-L1 were subcloned into a pFastBac vector and were expressed in SF9 cells. All proteins were purified by using a HisTrap excel column (GE Healthcare Life Sciences) following the product recommendations. Recombinant C-terminal His_{10}-tagged mouse PD-1 extracellular domain was purchased from Sino Biological.

The 2B4 TCR V_mC_h chimeras containing an engineered C domain disulfide were cloned into the pAcGP67a insect expression vector (554756; BD Biosciences) encoding either a C-terminal acidic GCN4-zipper-Biotin acceptor peptide (BAP)-His_6 tag (for the α chain) or a C-terminal basic GCN4 zipper-His_6 tag (for the β chain) (41). Thus, the resulting dimer has a combined His_{12}. Each chain also encoded a 3C protease site between the C terminus of the TCR ectodomains and the GCN4 zippers to allow for cleavage of zippers. IE^k MHC was cloned into pAcGP67A with acidic/basic zippers and His tags as described for TCRs. IE^k α and 2B4 α chains also encoded the ybbR-tag sequence for direct protein labeling. The IE^kβ construct was modified with an N-terminal extension containing either the 2A peptide via a Gly-Ser linker or the CLIP peptide via a Gly-Ser linker containing a thrombin cleavage site. Proteins were transiently expressed in High Five insect cells (BTI-TN-5B1-4) and purified using His-tag/Nickel affinity chromatography according to published protocols (25).

For fluorescent labeling of SNAP-tagged proteins, 10 μM protein was incubated with 20 μM benzylguanine functionalized dye (New England Biolabs) in HBS buffer [50 mM Hepes, 150 mM NaCl, 1 mM Tris(2-carboxyethyl)phosphine (TCEP), pH 7.4] for 1 h at room temperature or overnight on ice. For PD-L1 and TCR, 10 μM protein was incubated with 30 μM tetramethylrhodamine-5-maleimide in HBS buffer for 1 h at room temperature. Excess dyes were removed using Zeba Spin Desalting Columns (89882; Thermo Fisher).

Preparation of SNAP-DNA Tethers. Oligonucleotides with a 3′/5′ terminal amine were ordered from IDT and labeled with BG-GLA-NHS as previously described (42). The adhesion strands used in this study consisted of a 3′ 20mer region (5′-ACTGACTGACTGACTGACTG-3′) with a 5′ 80mer poly-dT and the complementary sequence (5′- CAGTCAGTCAGTCAGTCAGT-3′) also with a 5′ 80mer poly-dT. Conjugation to benzyl-guanine was performed as described (42). His_{10}-tagged SNAP was labeled at a concentration of 5 μM with a threefold excess of BG-DNA in HBS (50 mM Hepes, 150 mM NaCl, and 1 mM TCEP, pH 7.4).

Electroformation of GUVs. Lipids were mixed with a molar composition of 94.9% POPC, 5% DGS-NTA, 0.1% DOPE-390 in chloroform (12550; Electron Microscopy Sciences) and dried under vacuum for 1 h to overnight. Electroformation was performed in 370 mM sucrose according to published protocols (43). GUVs were stored at room temperature and imaged within 1 wk.

Preparation of SLBs. Small unilamellar vesicles (SUVs) were prepared from a mixture of 97.5% POPC, 2% DGS-NGA-Ni, and 0.5% PEG5000-PE. The lipid mixture in chloroform was evaporated under argon and further dried under vacuum. The mixture was rehydrated with PBS (pH 7.4), cycled between −80 °C and 37 °C 20 times, and then centrifuged for 45 min at 35,000 relative centrifugal force. SUVs made by this method were stored at 4 °C and used within 2 wk of formation. SLBs were formed in freshly plasma-cleaned custom poly(dimethylsiloxane) (PDMS) chambers on RCA-cleaned glass coverslips. One hundred microliters of SUV solution containing 0.5–1 mg/mL lipid were added to the coverslips and incubated for 30 min. Unadsorbed vesicles were removed, and bilayers were blocked by washing three times with reaction buffer (50 mM Hepes, 150 mM NaCl, 1 mM TCEP, 1 mg/mL BSA, pH 7.4), and incubating for 20 min.

Optical Setup for Spinning Disk, TIRF, and SAIM. Imaging was performed on one of two Nikon TI-E microscopes equipped with a Nikon 60× Plan Apo VC 1.20 NA water immersion objective or a Nikon 100× Plan Apo 1.49 NA oil immersion objective and four laser lines (405, 488, 561, and 640 nm), either a Hamamatsu Flash 4.0 or an Andor iXon EM-CCD camera, and μManager software (44). A polarizing filter was placed in the excitation laser path to polarize the light perpendicular to the plane of incidence. The angle of illumination was controlled with either a standard Nikon TIRF motorized positioner or a mirror moved by a motorized actuator (CMA-25CCCL; Newport). Scanning angle microscopy was performed and analyzed as previously described (45). For FRAP experiments, a region of ∼1 μm^2 was photobleached using a 405-nm laser modulated by a Rapp UGA-40 photo-targeting unit, and the fluorescence recovery was monitored over time.

Reconstitution of Membrane Interfaces. GUVs and SLBs were separately incubated for 1 h with the indicated proteins for each experiment. Proteins were diluted in reaction buffer (50 mM Hepes, 150 mM NaCl, 1 mM TCEP, 1 mg/mL BSA, pH 7.4) and then were mixed 2:1 with GUVs or were added to SLBs. SLBs were washed six times with one-half of the total well volume, resulting in a final concentration of ∼1% input protein remaining. The GUVs were not washed but were diluted 10-fold into the imaging well with the SLB after 1-h incubation. Rapamycin (R0395; Sigma) was added to FRB–FKBP reactions at a final concentration of 5 μM. GUVs were allowed to settle for 30–60 min before imaging. SLB fluidity was assessed by visualizing the diffusion of unbound GUV proteins that associate with

the SLB (e.g., FKBP, TCR, CD45). If >25% of the fluorescent molecules on the SLB were not diffusive, the experiment was repeated with a more fluid bilayer.

Estimated Protein Densities. Protein densities are estimates based on the conversion factor between protein concentration and molecular density defined by Schmid, et al. (16). Given that our system utilizes a physical setup analogous to their experiments, including the same homemade PDMS wells with a 100-uL volume (described in *Preparation of the SLBs* above) and protein concentrations in a similar range (1–100 nM), we can extrapolate from their measurement of 2,317 ± 370 molecules/μm^2 for an SLB with 2.5% DGS-NTA-Ni incubated with 100 nM His_{10}-tagged protein. Because the SLBs used in this study contain 2% DGS-NTA-Ni and GUVs contain 5% DGS-NTA-Ni, this factor (23.17 molecules·μm^{-2}·nM^{-1}) was first multiplied by 0.8 or 2, respectively. Protein concentrations (in nanomolars) were then multiplied by the membrane-specific scaling factor to give an estimated final density in molecules per square micrometer. This estimate may be imperfect due to differences in specific experimental variables affecting the total lipid surface area available for protein binding, including differences in electroformation. These estimated densities are 5–200 molecules/μm^2 for FKBP, 1,000 molecules/μm^2 for CD45 R0 and RABC, 200 molecules/μm^2 for TCR, 50 molecules/μm^2 for PD-L1, 50 molecules/μm^2 for SNAP, 100–300 molecules/μm^2 for PD-1, 200 molecules/μm^2 for MHC, and 20 molecules/μm^2 for FRB.

Image Analysis. Images were analyzed using ImageJ (Fiji) (46). The same brightness and contrast were applied to images within the same panels. Fiji rolling ball background subtraction was applied to images before calculating mean fluorescence intensities. Percent exclusion was calculated as one minus the ratio of average intensity inside a receptor-enriched zone to the average intensity at the interface outside the receptor-enriched zone. Regions of interest inside and outside receptor-enriched zones were selected manually within regions of comparable lipid intensity. "All exclusion quantification" refers to images acquired using TIRF microscopy. Data from image analysis within Fiji were graphed using Microsoft Excel.

Liposome Assay. Experiments were carried out as previously described (28). Briefly, proteins were purified using a baculovirus- or bacterial-expression system. Large unilamellar vesicles (LUVs) and proteins of interest were premixed and incubated at room temperature for 1 h. Then 2 mM ATP was injected and rapidly mixed to trigger Lck-mediated phosphorylation of CD3ζ and PD-1. Twenty minutes after ATP addition, apyrase was added ($t = 0$ min), and the reactions were allowed to continue at room temperature. Equal fractions of the reactions were removed and terminated with SDS sample buffer at the indicated time points. Anti-phosphotyrosine antibody (pY20, Santa Cruz Biotechnology; SC-508) was used to detect phosphorylation by Western blotting.

ACKNOWLEDGMENTS. We thank N. Stuurman for help with microscopy and image analysis, M. Taylor for guidance with protein purification and DNA tethering, and A. Williamson, N. Stuurman, and M. Morrissey for comments on the manuscript. Funding was provided by the Howard Hughes Medical Institute and NIH Grant R01EB007187 (to R.D.V.).

1. Carbone CB, et al. (June 7, 2017) In vitro reconstitution of T cell receptor-mediated segregation of the CD45 phosphatase. bioRxiv, 10.1101/097600.
2. Brownlie RJ, Zamoyska R (2013) T cell receptor signalling networks: Branched, diversified and bounded. *Nat Rev Immunol* 13:257–269.
3. Davis SJ, van der Merwe PA (2006) The kinetic-segregation model: TCR triggering and beyond. *Nat Immunol* 7:803–809.
4. Woollett GR, Williams AF, Shotton DM (1985) Visualisation by low-angle shadowing of the leucocyte-common antigen. A major cell surface glycoprotein of lymphocytes. *EMBO J* 4:2827–2830.
5. McCall MN, Shotton DM, Barclay AN (1992) Expression of soluble isoforms of rat CD45. Analysis by electron microscopy and use in epitope mapping of anti-CD45R monoclonal antibodies. *Immunology* 76:310–317.
6. Chang VT, et al. (2016) Initiation of T cell signaling by CD45 segregation at 'close contacts'. *Nat Immunol* 17:574–582.
7. Garcia KC, et al. (1996) An alphabeta T cell receptor structure at 2.5 Å and its orientation in the TCR-MHC complex. *Science* 274:209–219.
8. Choudhuri K, Wiseman D, Brown MH, Gould K, van der Merwe PA (2005) T-cell receptor triggering is critically dependent on the dimensions of its peptide-MHC ligand. *Nature* 436:578–582.
9. Leupin O, Zaru R, Laroche T, Müller S, Valitutti S (2000) Exclusion of CD45 from the T-cell receptor signaling area in antigen-stimulated T lymphocytes. *Curr Biol* 10: 277–280.
10. Johnson KG, Bromley SK, Dustin ML, Thomas ML (2000) A supramolecular basis for CD45 tyrosine phosphatase regulation in sustained T cell activation. *Proc Natl Acad Sci USA* 97:10138–10143.
11. Varma R, Campi G, Yokosuka T, Saito T, Dustin ML (2006) T cell receptor-proximal signals are sustained in peripheral microclusters and terminated in the central supramolecular activation cluster. *Immunity* 25:117–127.
12. James JR, Vale RD (2012) Biophysical mechanism of T-cell receptor triggering in a reconstituted system. *Nature* 487:64–69.
13. Cordoba S-P, et al. (2013) The large ectodomains of CD45 and CD148 regulate their segregation from and inhibition of ligated T-cell receptor. *Blood* 121:4295–4302.
14. Lee S-JE, Hori Y, Chakraborty AK (2003) Low T cell receptor expression and thermal fluctuations contribute to formation of dynamic multifocal synapses in thymocytes. *Proc Natl Acad Sci USA* 100:4383–4388.
15. Weikl TR, Lipowsky R (2004) Pattern formation during T-cell adhesion. *Biophys J* 87: 3665–3678.
16. Schmid EM, et al. (2016) Size-dependent protein segregation at membrane interfaces. *Nat Phys* 12:704–711.
17. Chung M, Koo BJ, Boxer SG (2013) Formation and analysis of topographical domains between lipid membranes tethered by DNA hybrids of different lengths. *Faraday Discuss* 161:333–345, discussion 419–459.
18. Banaszynski LA, Liu CW, Wandless TJ (2005) Characterization of the FKBP.rapamycin. FRB ternary complex. *J Am Chem Soc* 127:4715–4721.
19. Taylor MJ, Husain K, Gartner ZJ, Mayor S, Vale RD (2017) A DNA-based T cell receptor reveals a role for receptor clustering in ligand discrimination. *Cell* 169:108–119.e20.
20. Chi Q, Wang G, Jiang J (2013) The persistence length and length per base of single-stranded DNA obtained from fluorescence correlation spectroscopy measurements using mean field theory. *Physica A* 392:1072–1079.
21. Gautier A, et al. (2008) An engineered protein tag for multiprotein labeling in living cells. *Chem Biol* 15:128–136.
22. Hermiston ML, Xu Z, Weiss A (2003) CD45: A critical regulator of signaling thresholds in immune cells. *Annu Rev Immunol* 21:107–137.
23. Carbone CB, Vale RD, Stuurman N (2016) An acquisition and analysis pipeline for scanning angle interference microscopy. *Nat Methods* 13:897–898.
24. Liang J, Choi J, Clardy J (1999) Refined structure of the FKBP12-rapamycin-FRB ternary complex at 2.2 A resolution. *Acta Crystallogr D Biol Crystallogr* 55:736–744.
25. Birnbaum ME, et al. (2014) Deconstructing the peptide-MHC specificity of T cell recognition. *Cell* 157:1073–1087.
26. Gascoigne NRJ, Zal T, Alam SM (2001) T-cell receptor binding kinetics in T-cell development and activation. *Expert Rev Mol Med* 2001:1–17.
27. Chen L, Flies DB (2013) Molecular mechanisms of T cell co-stimulation and co-inhibition. *Nat Rev Immunol* 13:227–242.
28. Hui E, et al. (2017) T cell costimulatory receptor CD28 is a primary target for PD-1–mediated inhibition. *Science* 355:1428–1433.
29. Kamphorst AO, et al. (2017) Rescue of exhausted CD8 T cells by PD-1–targeted therapies is CD28-dependent. *Science* 355:1423–1427.
30. Yokosuka T, et al. (2012) Programmed cell death 1 forms negative costimulatory microclusters that directly inhibit T cell receptor signaling by recruiting phosphatase SHP2. *J Exp Med* 209:1201–1217.
31. Sheppard K-A, et al. (2004) PD-1 inhibits T-cell receptor induced phosphorylation of the ZAP70/CD3ζ signalosome and downstream signaling to PKCtheta. *FEBS Lett* 574:37–41.
32. Lin DY, et al. (2008) The PD-1/PD-L1 complex resembles the antigen-binding Fv domains of antibodies and T cell receptors. *Proc Natl Acad Sci USA* 105:3011–3016.
33. Butte MJ, Peña-Cruz V, Kim M-J, Freeman GJ, Sharpe AH (2008) Interaction of human PD-L1 and B7-1. *Mol Immunol* 45:3567–3572.
34. Burroughs NJ, Wülfing C (2002) Differential segregation in a cell-cell contact interface: The dynamics of the immunological synapse. *Biophys J* 83:1784–1796.
35. Krobath H, Różycki B, Lipowsky R, Weikl TR (2011) Line tension and stability of domains in cell-adhesion zones mediated by long and short receptor-ligand complexes. *PLoS One* 6:e23284.
36. Hui E, Vale RD (2014) In vitro membrane reconstitution of the T-cell receptor proximal signaling network. *Nat Struct Mol Biol* 21:133–142.
37. Chui D, Ong CJ, Johnson P, Teh HS, Marth JD (1994) Specific CD45 isoforms differentially regulate T cell receptor signaling. *EMBO J* 13:798–807.
38. Czyzyk J, Leitenberg D, Taylor T, Bottomly K (2000) Combinatorial effect of T-cell receptor ligation and CD45 isoform expression on the signaling contribution of the small GTPases Ras and Rap1. *Mol Cell Biol* 20:8740–8747.
39. Okumura M, et al. (1996) Comparison of CD45 extracellular domain sequences from divergent vertebrate species suggests the conservation of three fibronectin type III domains. *J Immunol* 157:1569–1575.
40. Köster DV, Mayor S (2016) Cortical actin and the plasma membrane: Inextricably intertwined. *Curr Opin Cell Biol* 38:81–89.
41. Wilson DB, et al. (1999) Immunogenicity. I. Use of peptide libraries to identify epitopes that activate clonotypic CD4+ T cells and induce T cell responses to native peptide ligands. *J Immunol* 163:6424–6434.
42. Farlow J, et al. (2013) Formation of targeted monovalent quantum dots by steric exclusion. *Nat Methods* 10:1203–1205.
43. Schmid EM, Richmond DL, Fletcher DA (2015) Reconstitution of proteins on electroformed giant unilamellar vesicles. *Methods Cell Biol* 128:319–338.
44. Edelstein A, Amodaj N, Hoover K, Vale R, Stuurman N (2010) Computer control of microscopes using μManager. *Curr Protoc Mol Biol*, 10.1002/0471142727.mb1420s92.
45. Carbone CB, Vale RD, Stuurman N (2016) A data acquisition and analysis pipeline for scanning angle interference microscopy. *Nat Methods* 13:897–898.
46. Schindelin J, et al. (2012) Fiji: An open-source platform for biological-image analysis. *Nat Methods* 9:676–682.